AIAA Journal
Vol. 46, No. 1, January 2008

Pressure-Sensitive Paint Measurement of Pressure Distribution in a Supersonic Micronozzle

H. Nagai,* R. Naraoka,† K. Sawada,‡ and K. Asai‡
Tohoku University, Sendai 980-8579, Japan

DOI: 10.2514/1.28371

Micronozzles have recently commanded considerable attention because of their potential applications, such as in flow control of microspacecraft. It is difficult to understand fundamental physical phenomena in microscale flow due to the lack of suitable quantitative measurement tools (pressure and temperature sensors, etc.). Pressure-sensitive paint is one of the most promising options for global distribution measurement in microscale flow. In this paper, pressure distribution in a supersonic micronozzle with a nozzle throat of 250 μm was investigated using pressure-sensitive paint, and the experimental results were compared with numerical simulation by Reynolds-averaged Navier–Stokes equations in three-dimensional space. The pressure-sensitive paint measurement technique demonstrated its validity for quantitative measurement of pressure distribution in microscale flow and revealed that the performance of the present micronozzle is critically affected by the boundary layer along the side wall.

Nomenclature

I = photoluminescent intensity
Kn = Knudsen number
L = total length of nozzle
M = Mach number
P = pressure
Re = Reynolds number
T = temperature
x = distance from inlet of nozzle

Subscripts

ref = reference
0 = initial state at nozzle inlet

I. Introduction

THE recent development of a microsatellite, or microspacecraft, has attracted considerable attention in aerospace engineering. A microspacecraft has the potential to conduct difficult missions that cannot be achieved by the usual size spacecraft, at low cost and low risk. The growth of microelectromechanical systems (MEMS) technology is adaptable to needs and technologies for greater sophistication and diversity of the microspacecraft [1–9]. MEMS devices are widely used in fields such as fluid mechanics, heat transfer, and propulsion. In the aerospace field, engineers are interested in applications for microdevices such as microjets, microactuators, and micronozzles. A small-sized nozzle can be used for attitude adjustment and propulsion of micro- and nanosatellites or minispacecraft.

However, because of a lack of understanding about microscale flow, devices based on MEMS technology may not always operate as designed. A flow with a low Reynolds number and high Knudsen number is realized because the characteristic length of objects is small in a microscale device. In such a flowfield, the data in macrofield experiments are not necessarily applicable to the microscale device field. Improvement of prediction accuracy and reliability cannot be accomplished only with computational fluid dynamics (CFD), which gives results as a practical design tool in the "macro" region, for the design of microscale devices because its verification by experiment is indispensable.

In the design of MEMS, the system construction and fabrication technology has been done ahead of acquiring a grasp of the physical phenomena in microscale flow. To optimize the MEMS device design, it is necessary to conduct experiments that correctly simulate physical phenomena, and to understand the phenomena in detail. Therefore, there is a pressing need to develop microscale flow diagnosis technology. However, this is hampered by a lack of suitable quantitative measurement tools (pressure and temperature sensors, etc.). Most of the sensors applied to MEMS device measurement have limited resolution restricted by sensor size and device geometry. Pressure-sensitive paint (PSP) [10–16] is one of the most promising options for global distribution measurement in MEMS devices. PSP is a "molecular sensor," which is characterized by small molecular size of luminophores, so that it can be easily applied in microdevices, and provides more detailed information. Some experiments have been conducted using PSP for microscale flow [17–20]. However, there are few cases in which the experimental results taken by the PSP technique were compared in detail with the three-dimensional CFD results.

In the present experiment, we demonstrate the use of the PSP technique for quantitative measurement of pressure distribution in supersonic micronozzles with a nozzle throat of 250 μm, such as those that might be employed for flow control and/or small satellite orbit maintenance. In addition, the flowfield in a micronozzle is investigated multilaterally by comparing the experimental results with the CFD results. This paper aims to establish the flow diagnosis technology and to clarify the phenomena related to low Reynolds and high Knudsen flows that appear in microscale.

II. PSP Measurement Technique

PSP is an optical measurement technique that uses a photochemical phenomenon known as luminescence quenched by oxygen molecules. A schematic illustration of PSP measurement is shown in Fig. 1. Luminophores, whose ability to luminesce is inhibited by oxygen, are contained within the paint. Higher local concentration of oxygen results in lower photoluminescent intensity. Likewise, lower oxygen concentration results in higher intensity.

Presented as Paper 1046 at the 44th AIAA Aerospace Sciences Meeting and Exhibit, Reno, Nevada, 9–12 January 2006; received 16 October 2006; revision received 24 April 2007; accepted for publication 19 July 2007.

*Assistant Professor, Department of Aerospace Engineering. AIAA Member.

†Graduate Student, Department of Aerospace Engineering, Institute of Fluid Science.

‡Professor, Department of Aerospace Engineering. Associate Fellow AIAA.

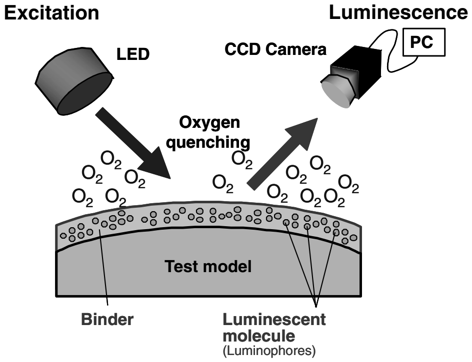

Fig. 1 Schematic illustration of PSP measurement.

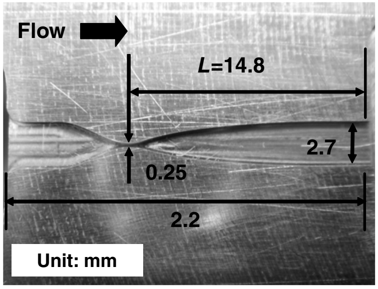

Fig. 2 Photo of micronozzle.

The Stern–Volmer relationship is used to relate change in intensity to pressure. This relationship can be expressed as

$$\frac{I_{\mathrm{ref}}}{I} = A(T) + B(T)\frac{P}{P_{\mathrm{ref}}} \tag{1}$$

where I_{ref} and P_{ref} are the luminescent intensity and static pressure obtained at a reference condition (wind-off), respectively. Intensity I, measured at a desired test condition (wind-on), is then used to calculate pressure P. Coefficients A and B are temperature-dependent values that are generally obtained by testing a coupon in a calibration chamber. To make absolute pressure measurements, the surface temperature must be known to define the local values of A and B.

III. Experimental Setup

A. Micronozzle and Optical Setup

Figure 2 shows a micronozzle made of aluminum used in the present experiment. A planar nozzle was used as a test case because the geometry is easy to visualize the inside of a nozzle, though an axisymmetric nozzle was used on actual microspacecraft [21,22]. It was fabricated with a high-accuracy computerized numerically controlled machine and the design Mach number M of the nozzle is 4.0. The nozzle shape was calculated by the method of characteristics. The inlet height is 2.70 mm and the throat height is 250 μm. The geometry of the throat at the micronozzle is measured by the confocal laser scanning microscope, shown in Fig. 3. To investigate the effect of boundary-layer growth, depths of 250 and 500 μm were used. The design parameters are summarized in Table 1.

PSP is painted on a glass plate with a spray gun, and the glass was fixed on the surface of a nozzle block with the glue so that the painted side of glass might become the inner wall of the nozzle, shown in Fig. 4. In addition, two thermocouples are mounted on the glass to measure the temperature of the model.

A photo of the experimental setup for the PSP measurement is shown in Fig. 5, and a schematic illustration is shown in Fig. 6. The exit of the nozzle is connected to a vacuum tank, and the back pressure was controlled to keep the pressure constant using a pressure regulator (Druck Limited, DPI 515). The pressure of the nozzle inlet was changed from atmospheric pressure to low pressure by controlling flowing quantity with the valve installed on the left. The pressure of the nozzle inlet and the back pressure were measured by using a pressure transducer (Kulite XT-190-25D).

The excitation light source for PSP was used as a UV-emitting light-emitting diode (LED) with a peak wavelength of 395 nm that was suitable for exciting PSP in the present test. An optical bandpass filter of $\lambda = 400 \pm 50$ nm was placed in front of the illuminator to cut undesirable near-infrared light. The luminescence on the model was captured by a thermoelectrically cooled 12-bit charge-coupled device (CCD) camera (Hamamatsu ORCA-ER, C4742-95) with 1024 × 1024 pixels resolution and 12-bit A/D resolution through a bandpass filter of $\lambda = 650 \pm 50$ nm.

B. PSP Formulation

The PSP used for this test employs platinum tetra (pentafluorophenyl) porphyrin (PtTFPP) as a probe molecule, and Poly (IBM-co-TFEM) [23] as an oxygen-permeable polymer binder. PtTFPP is commonly used as a pressure sensor because of its high quantum efficiency and low photodegradation. The peak absorbance is at a wavelength of approximately 395 and 530 nm, and the emission peak is 650 nm, shown in Fig. 7. Poly (IBM-co-TFEM) is a fluorinated copolymer suitable for use with PtTFPP. These materials

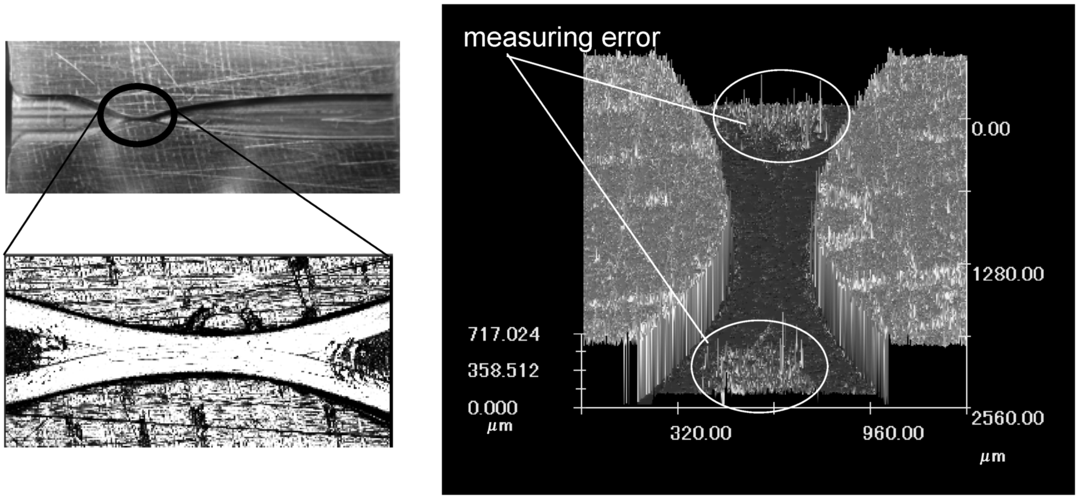

Enlarged part of nozzle throat

Surface roughness

Fig. 3 Geometry of throat at micronozzle is measured by confocal laser scanning microscope.

Table 1 Design parameters of micronozzle

Parameter	Value
Mach number, M	4.0
Total length, L	22.0 mm
Inlet height	2.7 mm
Outlet height	2.7 mm
Throat height	250 μm
Channel depth	500 or 250 μm

were dissolved in toluene. The dye concentration of the PSP was adjusted to maximize the luminescent intensity of PSP.

Figure 8a shows the properties of this combination, which is called the Stern–Volmer curve. It is seen that the pressure sensitivity is sufficiently high, but there is also some temperature sensitivity. In the present experiment, the pressure range is wide from the atmospheric pressure to about 1 kPa because the gas expands through a nozzle throat. For that purpose, the calibration was done enough to lower the pressure to 0.3 kPa, shown in Fig. 8b. It is seen that PSP has enough sensitivity from this figure in a low-pressure area.

C. Data Processing

In the present test, the gas temperature changes through a nozzle throat, hence it is necessary to correct a temperature effect in PSP measurement because there is a temperature dependency in the present paint. In the present experiment, the wind-on image I was taken during an airbreathing after the temperature of the nozzle was steady. And then, the wind-off reference image I_{ref} was taken just after an airbreathing of the nozzle stopped. The influence of the temperature distribution has been reduced by using the image of as similar temperature distribution as possible [24]. Five images were acquired in both the wind-off reference and the wind-on images, and averaged to reduce shot noise and readout noise. Both the wind-off reference image and wind-on images were compensated for dark images. Then, the image ratio I/I_{ref} was calculated and the temperature was corrected using a thermocouple mounted on the glass plate. Finally, the image ratio I/I_{ref} was transformed to a pressure image using the calibration characteristics, Eq. (1).

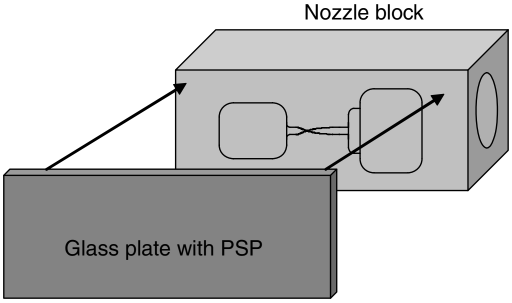

Fig. 4 Schematic illustration of fixing the glass plate with PSP to nozzle block.

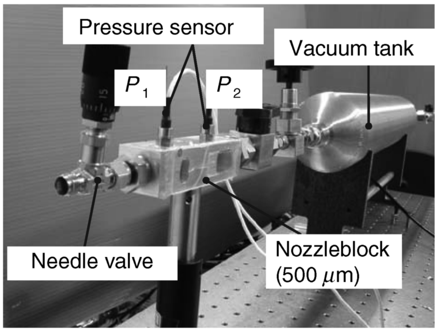

Fig. 5 Photo of experimental setup for PSP measurement.

IV. Numerical Method

To validate the PSP technique, we usually use data obtained with conventional electric sensors. However, in this experiment, the model was too small to place electric sensors. Therefore, we must compare the experimental results using PSP with the CFD results. Here, the surface pressure was estimated by Navier–Stokes (N.S.) code, using the same inflow conditions as in the experiment. The governing equations are the conventional Reynolds-averaged Navier–Stokes equations in three-dimensional space. The ideal gas equation of state is employed and the constant ratio of specific heat is assumed to be 1.4. We employ a two-equation model with the turbulent eddy viscosity. The turbulence model employed in this study is the q–w two-equation turbulence model developed by Coakley [25]. The governing equations are discretized using a conventional cell-centered finite volume scheme. A second-order spatial accuracy is attained by MUSCL approach. The equations are integrated in time by using the LU-SGS implicit scheme, which is known to have a time accuracy of less than unity. The Courant-Friedrichs-Lewy (CFL) number employed in this study was about unity. Numerical instability appeared when we attempted using a larger CFL number. The residual decreases for more than four orders of magnitude and then begins to fluctuate. The obtained solutions were judged converged.

We assume the constant upstream condition in the ghost cells adjacent to the inflow boundary. The numerical flux at the boundary surface is then determined by using the upwind scheme employed in the present study. At the exit boundary, we employ a zeroth order extrapolation from the interior values except for the pressure which is given as the boundary condition. The solid wall is assumed to be adiabatic and the nonslip boundary condition is enforced.

For three-dimensional computation, a structured computational mesh with $233 \times 61 \times 21$ grid points is used in the present calculations. For two-dimensional computation, the same numerical

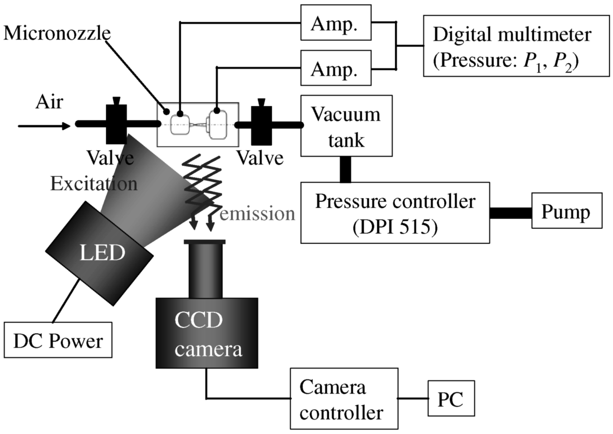

Fig. 6 Schematic illustration of experimental setup.

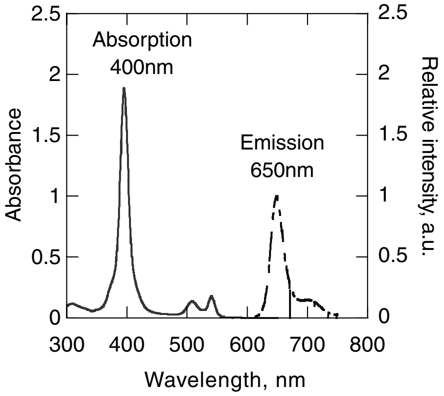

Fig. 7 Absorption and luminescence spectrum of PtTFPP.

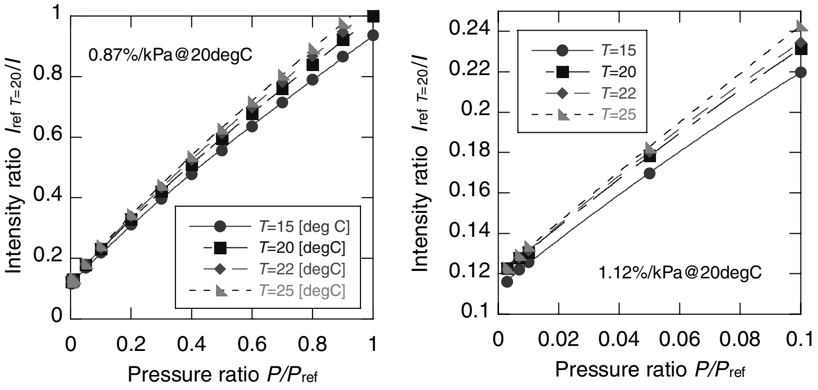

a) b)

Fig. 8 Stern–Volmer relation of PtTFPP/Poly (IBM-co-TFEM), $P_{\mathrm{ref}} = 100$ kPa: a) overall range from 100 to 0 kPa, b) low-pressure range from 10 to 0.3 kPa.

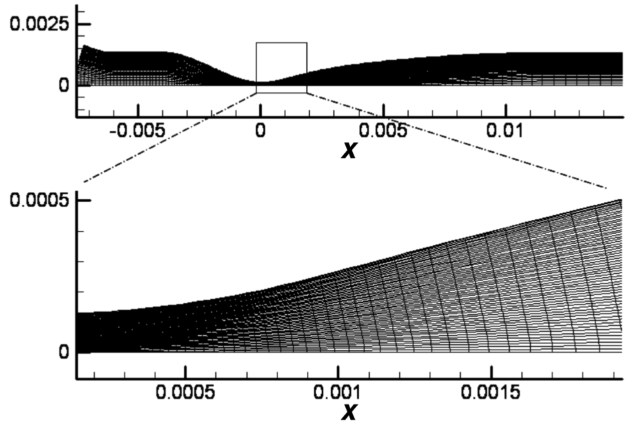

Fig. 9 Computational mesh in vertical symmetry plane with 233 × 61 grid points.

code is used with $233 \times 61 \times 2$ grid points. Figure 9 shows a computational mesh in the vertical symmetry plane for the three-dimensional case.

Before calculating all the cases, a grid refinement analysis in the two- and three-dimensional cases were performed with fine mesh, which are $233 \times 121 \times 41$ grid points for three-dimensional computation and $233 \times 121 \times 2$ grid points for two-dimensional computation. The minimum/maximum values of the mesh sizes in all directions for the final mesh are shown in Table 2.

The result of the grid analysis is shown in Fig. 10. It is found from the figure that the results are independent of the mesh size. Accordingly, the original mesh was used to shorten the calculating time in the present computation.

V. Results and Discussion

A. Experimental Results

The tests were conducted for six cases, as listed in Table 2. P_0 and T_0 are the total pressure and temperature at the nozzle inlet, respectively. Re and Kn are the Reynolds number and Knudsen number at the constant area supersonic region. The characteristic length is 2.7 mm. The Knudsen number for each case is smaller than 0.01, so that the flow can be treated as continuum flow in this experiment. Figure 10 shows a pressure map of supersonic flow in the micronozzle for case 1. First of all, it is seen that the pressure distribution in a microscale device, like the micronozzle, was able to be captured with PSP. The pressure distribution along the centerline of the nozzle is plotted in Fig. 11. The vertical axis indicates a static pressure normalized by the total pressure (P/P_0), x/L means a dimensionless length, and L is the length from nozzle throat to the end. The pressure change by the expansion of gas passing through the nozzle throat is clearly captured from this figure. The pressure decreases from the convergent section, passes through the throat at 0.528, and keeps decreasing at the divergent section until x/L equals 0.3, as calculated from one-dimensional isentropic flow analysis. However, a gradual pressure rise is seen in the constant region. The pressure at the nozzle exit is higher than that at the constant region.

Table 2 Mesh sizes in all directions

		Minimum × 10^{-5}, m	Maximum × 10^{-5}, m
Original mesh	flow direction	0.99	47.10
	wall direction	0.17	8.73
	depth direction	1.25	25.0
Fine mesh	flow direction	0.99	47.10
	wall direction	0.087	4.48
	depth direction	0.62	12.50

The comparison between PSP data and one-dimensional isentropic flow analysis is plotted in Fig. 12, where the total pressure $P_0 = 100$ kPa. The PSP data show the same trend as the isentropic flow analysis in the throat region, but the Mach number in the divergent region only increases up to 3.0, and then the flow starts slowing down. This difference can be attributed to boundary-layer growth, which is not accounted for in the isentropic flow analysis.

Figure 13 shows the Mach contour of supersonic flow for the all cases (case 1–case 6). Figure 14 is the Mach number distribution along the centerline of the nozzle for the six cases. First of all, it is understood from Fig. 13a that the Mach number is the highest in the center part of the downstream region of the nozzle, and the flow decelerates toward the exits of the nozzle from the center part. Furthermore, the Mach number distributions are almost symmetrical against the centerline of the nozzle. This result shows that the machining accuracy of the nozzle is enough.

Next, it is understood from these results in Figs. 13 that all cases show the same trend as Fig. 13a, but the Mach number in the downstream region decreases and the boundary layer grows as the total pressure P_0 decreases. It is seen from Fig. 14 that there is an increasing difference between the experimental results and the isentropic flow analysis. It is considered that the effect of the viscosity increases because the Reynolds number decreases with decreasing total pressure P_0, and the influence of the boundary layer on the flow becomes stronger. In cases 5 and 6, where the total pressure P_0 is low, the flow decelerates by the upstream part of the throat probably because of the boundary layer growing and filling the channel. Accordingly, the area of the nozzle becomes small somewhat, and influences the flow of the downstream part. Especially, the nozzle throat is almost filled in the boundary layer in case 6, and the downstream part has fallen very much into disorder.

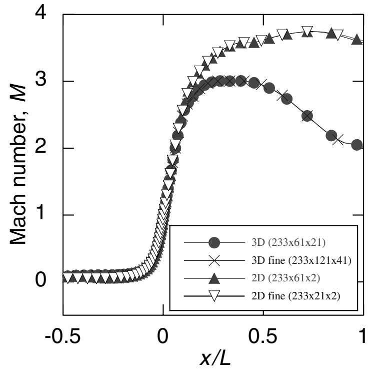

Fig. 10 Grid refinement analysis in the two- and three-dimensional computations.

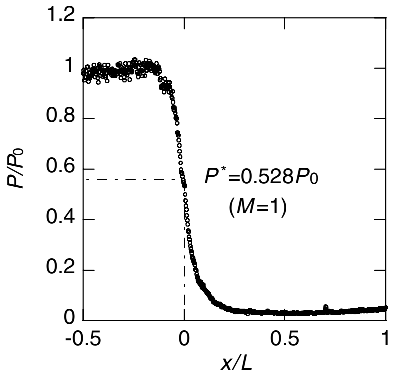

Fig. 11 Pressure distributions along the centerline of nozzle for case 1, normalized by the total pressure, $P_0 = 100$ kPa.

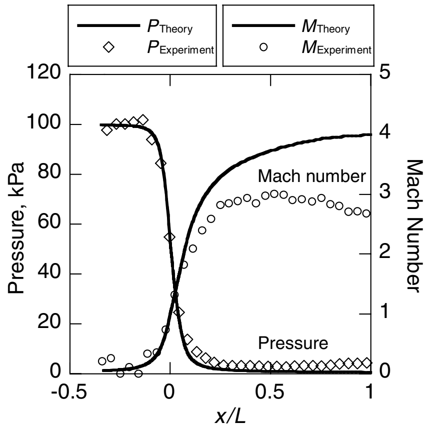

Fig. 12 Comparison of PSP data with isentropic flow analysis for case 1, $P_0 = 100$ kPa.

B. Comparison of Experimental Data and Numerical Results

To more fully understand the experimental results, they were compared with numerical simulations (two- and three-dimensional). The computations are made for two cases: case 1 and case 5. The chamber pressure is 100 and 20 kPa, respectively. The chamber temperature is kept constant at 300 K. At the exit of the nozzle, we enforce the zero-gradient exit condition for the dependent variables except for the pressure. In the present calculation, the back pressure is currently assumed to be 1/100 of the chamber pressure, namely 1000 and 200 Pa, respectively.

Figure 15 shows the experimental result and the numerical results in case 1. Figure 15a is the Mach contour of the experiment, Figs. 15b and 15c are three-dimensional and two-dimensional computations, respectively, and Fig. 15d is the Mach number distributions along the

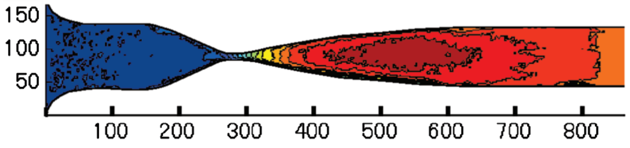

a) Case1=100kPa

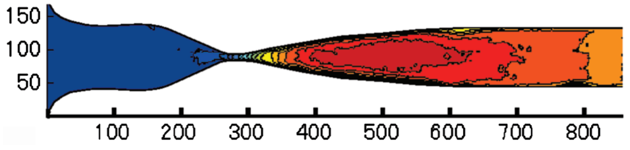

b) Case2=70kPa

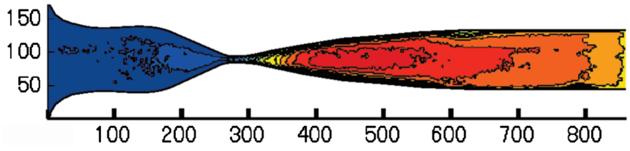

c) Case3=50kPa

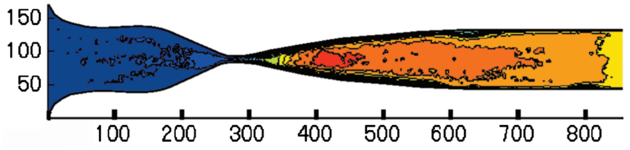

d) Case4=40kPa

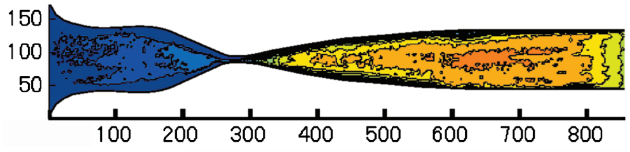

e) Case5=20kPa

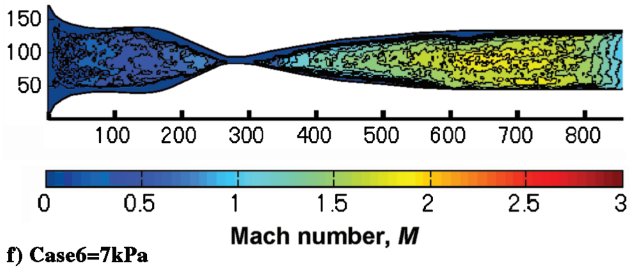

f) Case6=7kPa

Fig. 13 Mach contour of supersonic flow using intensity method for six cases in micronozzle.

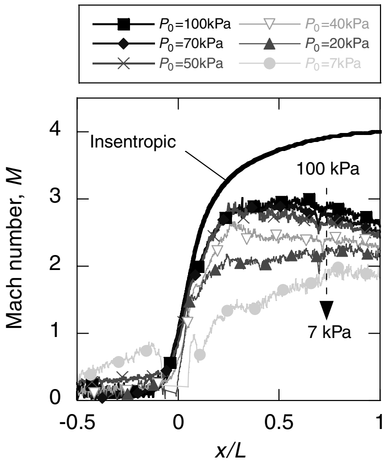

Fig. 14 Mach number distributions along the centerline of nozzle for six cases.

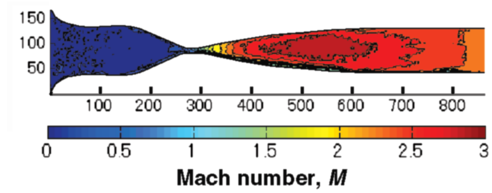

a) Experiment

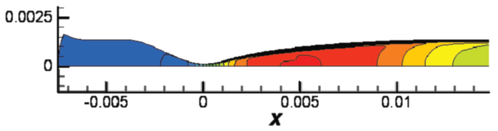

b) 3D-CFD

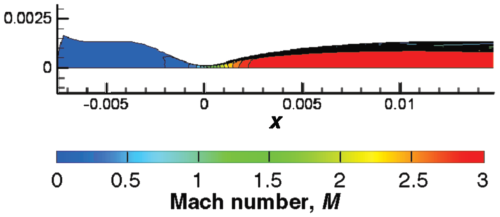

c) 2D-CFD

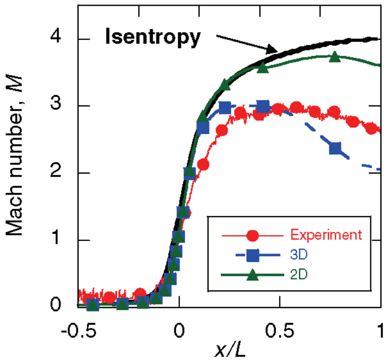

d) Mach number profile

Fig. 15 Experimental and numerical results of Mach contour for vertical symmetric plane in case 1 of $P_0 = 100$ kPa: a) experimental result, b) three-dimensional computation, c) two-dimensional computation, d) Mach number profiles along the centerline of nozzle.

centerline of the nozzle. First of all, the experiment result is compared with the three-dimensional computation result. It is seen from Figs. 15a and 15b that the three-dimensional computations give reasonable agreement with the experimental data for the Mach contour and the Mach number distribution. Especially, the maximum Mach numbers are almost the same, and rise up to about 3.0. However, the position of the maximum Mach number is the upstream sides compared with the experiment result, and it is understood that the flow has decelerated rapidly in the downstream region. On the other hand, the two-dimensional computation differs greatly from the experimental results and the three-dimensional computation; in fact, it is seen from Fig. 15d that the flow of the centerline of the nozzle hardly decelerates and the maximum Mach number became about 3.7 nearing an isentropy value, which is almost the same as the isentropic value. However, the boundary-layer growth in the two-dimensional computation is larger than the experimental result and three-dimensional computation result in the vicinity of the nozzle upper and lower wall. The Mach number of the two-dimensional computation result has become a little smaller than the isentropy value because of the development of this boundary layer.

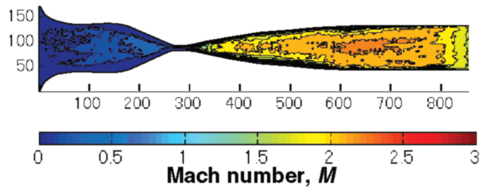

a) Experiment

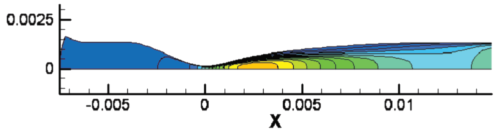

b) 3D-CFD

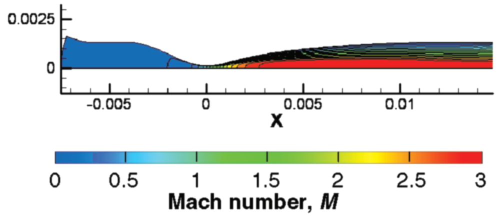

c) 2D-CFD

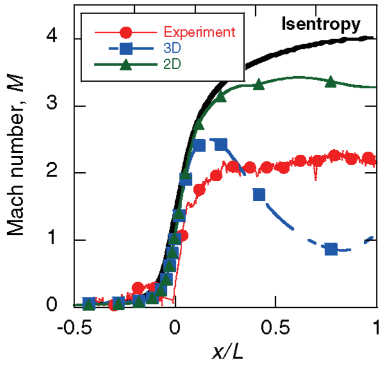

d) Mach number profile

Fig. 16 Experimental and numerical results of Mach contour for vertical symmetric plane in case 5 of $P_0 = 20$ kPa: a) experimental result, b) three-dimensional computation, c) two-dimensional computation, d) Mach number profiles along the centerline of nozzle.

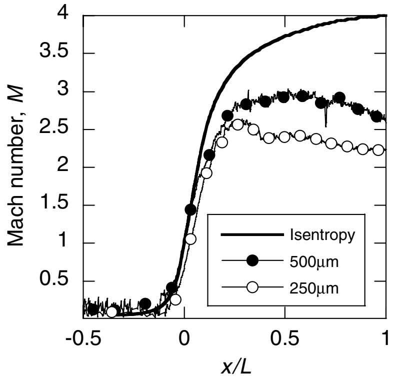

Fig. 17 Experimental results of Mach number profile along the centerline of nozzle for different channel depths of 250 and 500 μm.

Figure 16 shows the experimental result and the numerical results in case 5. Figure 16a is the Mach contour of experiment, Figs. 16b and 16c are three-dimensional and two-dimensional computations, respectively, and Fig. 16d is the Mach number distributions along the centerline of the nozzle. First of all, the experiment result is compared with the three-dimensional computation result. Contrary to case 1, the Mach number contour and distribution differs greatly from the experimental results. The maximum Mach number is about 2.2 in the experiment, whereas it is about 2.5 in the three-dimensional computation result. The position of the maximum Mach number is also different in the experiment and the three-dimensional

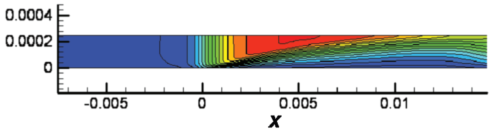

a) Case1: P_0=100kPa

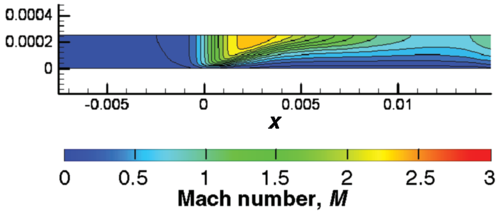

b) Case5: P_0 =20kPa

Fig. 18 Three-dimensional computation results of Mach contour for horizontal symmetric plane in cases 1 and 5.

computation results. In addition, it is the upstream sides compared with the experiment result and three-dimensional computation result of case 1. In the case of Fig. 16d, the deceleration of the flow is far larger than the experiment result. After the flow decelerates once in the constant region, it accelerates again in the vicinity of the nozzle exit. The reason for the reacceleration is that the back pressure in the experiment might be substantially higher than that assumed in the computation. In computation, the boundary condition of the back pressure is currently assumed to be $1/100$ of the chamber pressure, namely 200 Pa. The computational results are sensitive to the back pressure, and so the pressure in the constant region approaches the back pressure.

Then, the boundary-layer growth seems to be larger than the experimental result in the vicinity of the nozzle upper and lower wall, shown in Figs. 16a and 16b. The reason for this is that the computational model has employed a two-equation model with the turbulent eddy viscosity. It is considerably small in case 5, though the *Re* number is large in case 1, shown in Table 2. Accordingly, it seems that the laminar flow realizes in the micronozzle for case 5. Therefore, it is thought that the three-dimensional computation result differs from the experiment result in case 5, though there were not so many differences in case 1.

Next, the two-dimensional computation result in case 5 is discussed. It is seen from Fig. 16c that the boundary layer is growing very much compared with the result in case 1. As mentioned before, the effect of the viscosity became strong because the total pressure P_0 became small. However, in Fig. 16d, the influence of the boundary layer on the flow has not gone out as remarkably as the three-dimensional computation result owing to the Mach number profile along the centerline of nozzle. It is noted that the maximum Mach number becomes about 3.4, and has decreased by about 9% compared with Fig. 15c of case 1.

From a current comparison, the three-dimensional computations give reasonable agreement with the experimental data for both cases. On the other hand, the two-dimensional computation differs greatly from the experimental results and the three-dimensional computation; in fact, it is almost the same as the isentropic value. To investigate this reason, the experiment that used the nozzle with different channel depth was done. Figure 17 shows the Mach number distribution along the centerline of the nozzle with different channel depths of 250 and 500 μm. It was found that the difference in the shallower channel with the isentropic flow analysis is greater than that of the deeper channel. This means that the influence of the boundary layer from the side wall is stronger in the shallower channel case. Figure 18 shows the three-dimensional computation results of Mach contour for horizontal symmetric plane in cases 1 and 5. It is seen from these figures that the boundary layer develops remarkably along the sidewall of the nozzle. In case 5 with the $P_0 = 20$ kPa, the boundary layer reaches the sidewall at once after the flow passes through the nozzle throat. This causes the drastic deceleration of the flow for three-dimensional computation results in case 5. From the experimental and numerical results, we can say that the performance of the present micronozzle is critically affected by the boundary layer along the side wall.

VI. Conclusions

In the present study, the micronozzle was investigated using pressure-sensitive paint. We compared the experimental results with numerical simulation by CFD to validate the PSP measurement technique. The following conclusions were obtained from the experimental results:

1) The PSP measurement technique demonstrates its validity for quantitative measurement of pressure and Mach number distribution in supersonic micronozzles.

2) The effect of boundary-layer growth becomes dominant as the Reynolds number decreases with decreasing total pressure P_0.

3) Three-dimensional computations give reasonable agreement with the experimental data.

4) The performance of the present micronozzle is critically affected by the boundary layer along the side walls.

Acknowledgments

This work is partially supported by a Grant-in-Aid for Scientific Research (B) (16360419), Japan Society for the Promotion of Science. We express our sincere thanks to Chin-Yung Huang at Purdue University for contributing valuable discussion and to Tatsuya Osafune for designing the test models.

References

[1] Mueller, J., Tang, W., Wallace, A., Li, W., Bame, D., Chakraborty, I., and Lawton, R., "Design, Analysis and Fabrication of a Vaporizing Liquid Micro-Thruster," AIAA Paper 97-3054, 1997.

[2] Mueller, J., "Thruster Options for Microspacecraft: A Review and Evaluation of Existing Hardware and Emerging Technologies," AIAA Paper 97-3058, 1997.

[3] Zhang, K. L., Chou, S. K., Ang, S. S., and Tang, X. S., "A MEMS-Based Solid Propellant Microthruster with Au/Ti Igniter," *Sensors and Actuators A, Physical*, Vol. 122, No. 1, 2005, pp. 113–123. doi:10.1016/j.sna.2005.04.021

[4] Chen, K., Winter, M., and Huang, R. F., "Supersonic Flow in Miniature Nozzles of Planar Configuration," *Journal of Micromechanics and Microengineering*, Vol. 15, No. 9, 2005, pp. 1736–1744. doi:10.1088/0960-1317/15/9/016

[5] Jamison, A. J., and Ketsdever, D., "Low Reynolds Number Performance Comparison of an Underexpanded Orifice and a DeLaval Nozzle," *AIP Conference Proceedings, Rarefied Gas Dynamics: 23rd International Symposium*, Vol. 663, 2003, pp. 557–564.

[6] Chong, X., "Characteristics of Micronozzle Gas Flows," *Physics of Fluids*, Vol 19, March 2007, pp. 37–102. doi:10.1063/1.2709707

[7] Gadepalli, V., and Lin, C., "Navier–Stokes Modeling of Gas Flows in a DeLaval Micronozzle," *44th Aerospace Sciences Meeting and Exhibit*, AIAA Paper 2006-1425, 2006.

[8] Ketsdever, A. D., Clabough, M. T., Gimelshein, S. F., and Alexeenko, A. A., "Experimental and Numerical Determination of Micropropulsion Device Efficiencies at Low Reynolds Numbers," *AIAA Journal*, Vol. 43, No. 3, 2005, pp. 633–641.

[9] Alexeenko, A. A., Levin, D. A., Fedosov, D. A., Gimelshein, S. F., and Collins, R. J., "Performance Analysis of Microthrusters Based on Coupled Thermal-Fluid Modeling and Simulation," *Journal of Propulsion and Power*, Vol. 21, No. 1, 2005, pp. 95–101.

[10] Liu, T., Campbell, B. T., Burns, S. P., and Sullivan, J. P., "Temperature- and Pressure-Sensitive Luminescent Paints in Aerodynamics," *Applied Mechanics Reviews*, Vol. 50, No. 4, 1997, pp. 227–246.

[11] Bell, H. J., Schairer, T. E., Hand, A. L., and Mehta, R. D., "Surface Pressure Measurements Using Luminescent Coatings," *Annual Review of Fluid Mechanics*, Vol. 33, Jan. 2001, pp. 155–206. doi:10.1146/annurev.fluid.33.1.155

[12] Asai, K., Amao, Y., Iijima, Y., Okura, I., and Nishide, H., "Novel Pressure-Sensitive Paint for Cryogenic and Unsteady Wind-Tunnel Testing," *Journal of Thermophysics and Heat Transfer*, Vol. 16, No. 1, 2002, pp. 109–115.

[13] Niimi, T., Yoshida, M., Kondo, M., Oshima, Y., Mori, M., Egami, Y., Asai, K., and Nishide, H., "Application of Pressure-Sensitive Paints to Low Pressure Range," *Journal of Thermophysics and Heat Transfer*, Vol. 19, No. 1, 2005, pp. 9–16.

[14] Nakakita, K., Kurita, M., Mitsuo, K., and Watanabe, S., "Practical Pressure-Sensitive Paint Measurement System for Industrial Wind Tunnels at JAXA," *Measurement Science and Technology*, Vol. 17, No. 2, 2006, pp. 359–366.
doi:10.1088/0957-0233/17/2/017

[15] Klein, C., Engler, R. H., Henne, U., and Sachs, W. E., "Application of Pressure-Sensitive Paint for Determination of the Pressure Field and Calculation of the Forces and Moments of Models in a Wind Tunnel," *Experiments in Fluids*, Vol. 39, No. 2, 2005, pp. 475–483.
doi:10.1007/s00348-005-1010-8

[16] Mitsuo, K., Asai, K., Takahashi, A., and Mizushima, H., "Advanced Lifetime PSP Imaging System for Simultaneous Pressure and Temperature Measurement," *AIAA 24th Aerodynamic Measurements Technology and Ground Testing Conference*, AIAA Paper 2004-2188, June 2004.

[17] Huang, C. Y., Sakaue, H., Gregory, J. W., and Sullivan, J. P., "Molecular Sensors for MEMS," *40th Aerospace Sciences Meeting and Exhibit*, AIAA Paper 2002-0256, Jan. 2002.

[18] Huang, C. Y., and Sullivan, J. P., "Flow Visualization and Pressure Measurement in Micronozzles," *11th International Symposium on Flow Visualization*, Optimage, Edinburgh, 2004.

[19] Huang, C. Y., Gregory, J. W., Nagai, H., Asai, K., and Sullivan, J. P., "Molecular Sensors in Microturbine Measurement," *Proceedings of 2006 ASME International Mechanical Engineering Congress and Exposition on Disc* [CD-ROM], American Society of Mechanical Engineers, Paper IMECE2006_13814, 2006.

[20] Osafune, T., Kurotaki, T., and Asai, K., "Application of Molecular Sensors to Micro Objects in Supersonic Flow," *42nd Aerospace Sciences Meeting and Exhibit*, AIAA Paper 2004-1048, 2004.

[21] Mo, H., Lin, C., Gokaltun, S., and Skudarnov, P. V., "Numerical Study of Axisymmetric Gas Flow in Conical Micronozzles by DSMC and Continuum Methods," *44th Aerospace Sciences Meeting and Exhibit*, AIAA Paper 2006-991, 2006.

[22] Alexeenko, A. A., Levin, D. A., Gimelshein, S. F., Collins, R. J., and Reed, B. D., "Numerical Modeling of Axisymmetric and Three-Dimensional Flows in Microelectromechanical Systems Nozzles," *AIAA Journal*, Vol. 40, No. 5, 2002, pp. 897–904.

[23] Amao, Y., Asai, K., Miyashita, T., and Okura, I., "Photophysical and Photochemical Properties of Optical Oxygen Pressure Sensor of Platinum Porphyrin-Isobutylmethacrylate-Trifluoroethylmethacrylate Copolymer Film," *Polymer Journal*, Vol. 31, No. 12, 1999, pp. 1267–1296.
doi:10.1295/polymj.31.1267

[24] Yamashita, T., Sugiura, H., Nagai, H., Asai, K., and Ishida, K., "Pressure Sensitive Paint Measurement of the Flow Around a Simplified Car Model," *Journal of Visualization*, Vol. 10, No. 3, 2007, pp. 289–298.

[25] Coakley, T. J., "Turbulence Modeling Methods for the Compressible Navier–Stokes Equations, *16th Fluid and Plasma Dynamics Conference*, AIAA Paper 83-1693, 1983.

T. Jackson
Associate Editor